CELL BIOLOGY

FUBL-3/FUBP1 mediates mitochondrial stress–induced chromatin remodeling and longevity

Qian Zhang[1,2]†, Hangyu Dong[1,3]†, Yayun Jiang[1,3]†, Zihao Wang[1,3], Jiasheng Li[1,3], Ye Tian[1,3]*

Mitochondrial stress activates nuclear transcriptional programs to restore homeostasis and promote longevity; yet, the nuclear effector that directly reshapes chromatin during stress remains unclear. Through a forward genetic screen in *Caenorhabditis elegans*, we identify FUBL-3, the homolog of human far-upstream elements binding protein 1 (FUBP1), as a conserved regulator that couples mitochondrial stress to chromatin remodeling. FUBL-3 translocates to intestinal nuclei upon stress, where it drives nucleosome remodeling and deacetylase–dependent chromatin condensation and activates mitochondrial unfolded protein response (UPR^{mt}). Loss of *fubl-3* disrupts chromatin compaction and abolishes stress-induced lifespan extension, while its overexpression is sufficient to restructure chromatin, trigger UPR^{mt}, and extend lifespan. Notably, human FUBP1 rescues *fubl-3* mutants in worms and mediates chromatin remodeling in mammalian cells under mitochondrial stress. FUBP1 binds promoters of proteostasis and mitochondrial quality control genes, supporting its role in nuclear adaptation. Our study identifies FUBL-3/FUBP1 as a conserved mitochondrial-to-nuclear communicator that reprograms chromatin architecture to promote stress resilience and healthy aging.

INTRODUCTION

Mitochondria are central hubs that continuously communicate with the nucleus to orchestrate adaptive responses under stress. This retrograde mitochondria-to-nucleus signaling activates transcriptional programs essential for cellular homeostasis, survival, and organismal longevity. In *Caenorhabditis elegans*, such communication promotes stress resilience and lifespan extension, establishing it as a pivotal regulator of aging and systemic health (*1*–*8*). While mitochondrial stress is known to activate specific transcriptional programs such as the mitochondrial unfolded protein response (UPR^{mt}) (*9*–*11*), the broader reprogramming of nuclear chromatin architecture under mitochondrial stress, and its implications for organismal aging, remain largely uncharacterized.

Intriguingly, mitochondrial perturbations trigger dramatic chromatin reorganization, including global chromatin compaction and large-scale structural remodeling that enable a coordinated stress response. Although several nuclear factors, including the transcription factor DVE-1, the NuRD (nucleosome remodeling and deacetylase) complex, and epigenetic modifiers such as the H3K9me2 methyltransferase MET-2/LIN-65 and JMJD family members, have been implicated in this process (*12*–*15*). The core identity of a nuclear factor that is both necessary and sufficient to remodel chromatin in response to mitochondrial signals, and whether such mechanisms are conserved in mammals, has remained elusive.

We identified FUBL-3, the *C. elegans* homolog of human FUBP1 (far-upstream elements binding protein), as a conserved nuclear effector that directly links mitochondrial stress to chromatin remodeling. Through a forward genetic screen, we show that FUBL-3 translocates to intestinal nuclei upon mitochondrial perturbation, promotes NuRD-dependent chromatin condensation, activates UPR^{mt} genes, and extends lifespan. Overexpression of FUBL-3 is sufficient to induce chromatin compaction and longevity even in the absence of stress. In mammalian cells, FUBP1 mediates similar chromatin remodeling and stress-responsive transcription, and rescues *fubl-3* mutant phenotypes in worms. Chromatin profiling reveals that FUBP1 targets promoter-proximal regions of genes involved in proteostasis and mitochondrial quality control. These findings reveal a conserved mitochondrial-to-nuclear communication axis that reprograms chromatin architecture to promote longevity and systemic resilience, providing mechanistic insight into how organellar stress influences nuclear adaptation across species.

RESULTS

FUBL-3 is required for mitochondrial stress–induced nuclear responses

The UPR^{mt} is a conserved nuclear transcriptional program activated by mitochondrial dysfunction to restore proteostasis and maintain cellular resilience (*3*, *8*, *16*, *17*). In *C. elegans*, UPR^{mt} can be initiated both cell-autonomously and nonautonomously to orchestrate organism-wide adaptation (*18*–*22*). To identify regulators that transduce mitochondrial stress signals to the nucleus, we conducted a forward genetic screen using ethylmethane sulfonate (EMS) mutagenesis. We monitored UPR^{mt} activation by assessing the nuclear accumulation of a DVE-1::GFP (green fluorescent protein) translational reporter, a hallmark of stress-induced chromatin remodeling, in animals with neuronal expression of the Wnt ligand EGL-20 (*19*, *23*–*25*).

Among ~3400 mutagenized genomes, we identified 42 mutant lines in which DVE-1::GFP failed to accumulate in intestinal nuclei upon neuronal EGL-20 overexpression. Whole-genome sequencing revealed that three independent alleles *yth48*, *yth65*, and *yth66*, carried premature stop codons in the same gene, *fubl-3* (Fig. 1, A and B). Specifically, the nonsense mutations were Gln416stop (*yth48*), Trp493stop (*yth65*), and Gln570stop (*yth66*) (fig. S1A). Western blot analysis confirmed reduced DVE-1::GFP protein levels in all three *fubl-3* mutants (Fig. 1C), supporting a role for FUBL-3 in cell nonautonomous UPR^{mt} signaling. To further validate this finding, we

[1]Institute of Genetics and Developmental Biology, Chinese Academy of Sciences, Beijing 100101, China. [2]Key Laboratory of Cell Proliferation and Regulation Biology of the Ministry of Education, College of Life Sciences, Beijing Normal University, Beijing 100875, China. [3]University of Chinese Academy of Sciences, Beijing 100093, China.
*Corresponding author. Email: ytian@genetics.ac.cn
†These authors contributed equally to this work.

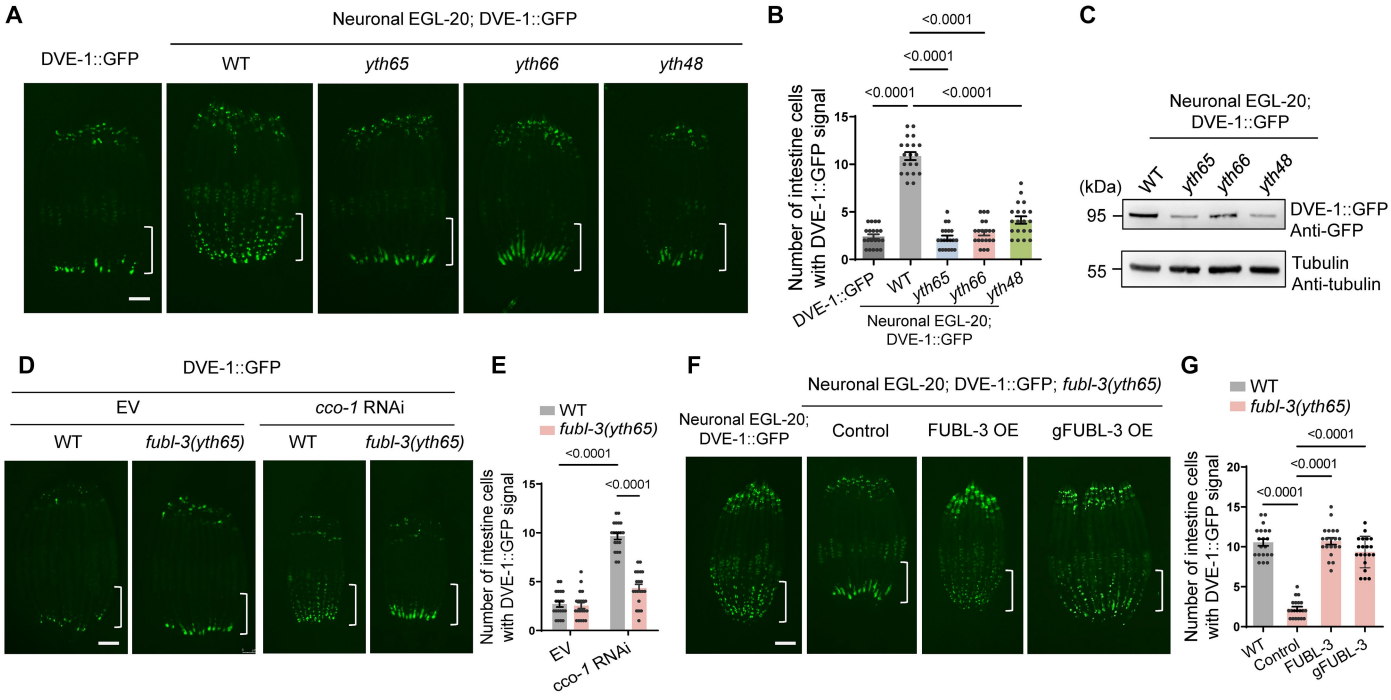

Fig. 1. FUBL-3 is required for mitochondrial stress–induced UPR^{mt} activation in *C. elegans*. (**A**) Representative images of DVE-1::GFP nuclear signal in posterior intestinal cells (bracketed) of day 1 adults across genotypes: wild-type (WT), neuronal EGL-20 overexpression, and neuronal EGL-20; *fubl-3* mutants (*yth65*, *yth66*, and *yth48*). (**B**) Quantification of intestinal nuclei with DVE-1::GFP foci in (A) [$n = 20$ worms; one-way analysis of variance (ANOVA)]. (**C**) Immunoblot of DVE-1::GFP and tubulin (loading control) in day 1 adults from (A). (**D**) Representative images of DVE-1::GFP in WT and *fubl-3(yth65)* animals treated with empty vector (EV) or *cco-1* RNAi. (**E**) Quantification of intestinal nuclei with DVE-1::GFP foci from (D) ($n = 20$ worms; two-way ANOVA). (**F**) Representative images of DVE-1::GFP signal in WT, *fubl-3(yth65)*, and *fubl-3(yth65)* animals rescued with pan-tissue or intestine-specific FUBL-3 expressing in neuronal EGL-20 overexpression background. (**G**) Quantification of intestinal nuclei with DVE-1::GFP foci from (F) ($n = 20$ worms; one-way ANOVA). Error bars represent SEM. Scale bar, 100 μm. See also fig. S1.

generated two additional *fubl-3* alleles (*yth70* and *yth71*) using CRISPR-Cas9 genome editing (fig. S1, A to C). Both alleles similarly impaired DVE-1::GFP nuclear localization in response to neuronal EGL-20 overexpression, as confirmed by imaging and western blotting (fig. S1D).

We next asked whether FUBL-3 is also required for cell-autonomous UPR^{mt} activation. In wild-type animals, RNA interference (RNAi)–mediated knockdown of *cco-1* (cytochrome C oxidase-1, a subunit of mitochondrial complex IV) robustly induced DVE-1::GFP nuclear accumulation. However, this response was markedly impaired in *fubl-3(yth65)* and *fubl-3(yth70)* mutants (Fig. 1, D and E). Consistently, induction of the UPR^{mt} reporter *hsp-6p::gfp* was significantly reduced in *fubl-3(yth65)* animals (fig. S1, E and F), and quantitative reverse transcription polymerase chain reaction (qRT-PCR) analysis confirmed that the up-regulation of endogenous *hsp-6* and *hsp-60* transcripts in response to *cco-1* RNAi was also suppressed (fig. S1G).

To assess the tissue-specific sufficiency of FUBL-3, we expressed FUBL-3 in *fubl-3(yth65)* mutants using either its endogenous promoter (*fubl-3p*) or the intestine-specific *gly-19p* promoter. Both transgenes fully restored DVE-1::GFP nuclear localization under mitochondrial stress (Fig. 1, F and G), indicating that intestinal expression of FUBL-3 is sufficient for cell-autonomous UPR^{mt} activation.

To determine whether FUBL-3 selectively regulates mitochondrial stress responses, we tested its role in other proteostasis pathways. In *fubl-3(yth65)* mutants, the endoplasmic reticulum (ER) stress reporter *hsp-4p::gfp* remained inducible by *hrd-1* RNAi, which impairs ER-associated degradation. Similarly, the cytosolic heat shock reporter *hsp-16.2p::gfp* (UPR^{HS}) was robustly induced following heat stress (fig. S1, H and I). These results suggest that *fubl-3* is not required for ER or cytosolic stress responses, highlighting its specificity for the mitochondrial UPR pathway. Collectively, these findings identify FUBL-3 as a critical and specific regulator of both non–cell autonomous and cell-autonomous UPR^{mt} activation, functioning upstream of DVE-1 to mediate nuclear transcriptional responses to mitochondrial perturbation.

Mitochondrial stress induces expression and nuclear accumulation of FUBL-3

To investigate how *fubl-3* is regulated in response to mitochondrial stress, we examined its expression and subcellular localization following mitochondrial perturbation. Using RNAi against *cco-1*, we observed a modest but consistent increase in the expression of a *fubl-3p::mCherry* transcriptional reporter, particularly in intestinal cells where mitochondrial stress reporters such as *hsp-6p::gfp* and DVE-1::GFP are most robustly induced (fig. S2, A and B). qPCR analysis further confirmed an up-regulation of endogenous *fubl-3* mRNA upon *cco-1* RNAi treatment (fig. S2C).

To assess FUBL-3 protein dynamics, we monitored a *fubl-3p::fubl-3::mCherry* translational reporter. Upon *cco-1* RNAi treatment, we observed a marked increase in FUBL-3 protein levels and its accumulation within intestinal nuclei (Fig. 2, A and B). A similar nuclear enrichment of FUBL-3::mCherry was observed in animals with neuronal EGL-20 overexpression, a non–cell autonomous trigger of

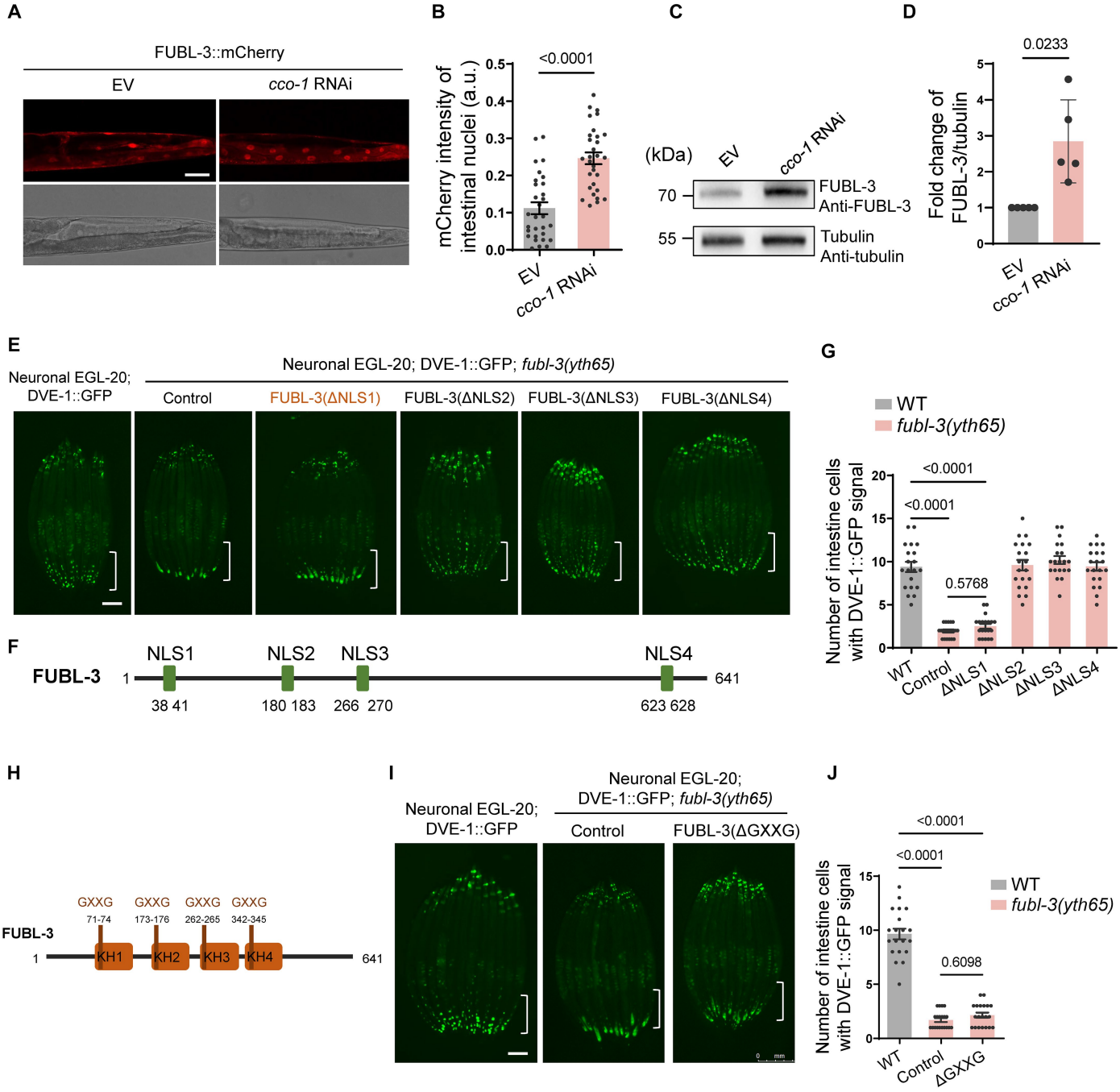

Fig. 2. Mitochondrial stress induces nuclear accumulation of FUBL-3. (**A**) Confocal images of FUBL-3::mCherry in day 1 adults with EV or *cco-1* RNAi. Scale bar, 50 μm. (**B**) Quantification of nuclear mCherry intensity in the intestine from (A) ($n = 30$ nuclei; two-tailed unpaired t test). (**C**) Immunoblot of FUBL-3 in day 1 adults treated with EV or *cco-1* RNAi. (**D**) Quantification of the FUBL-3 protein levels from (C) ($n = 5$ replicates; two-tailed paired t test). (**E**) Representative images of DVE-1::GFP signal in *fubl-3(yth65)* mutants rescued with wild-type or NLS-deleted FUBL-3 variants (ΔNLS1-4) under neuronal EGL-20 overexpression. Scale bar, 100 μm. (**F**) Schematic of predicted NLS in FUBL-3. (**G**) Quantification of intestinal nuclei with DVE-1::GFP foci from (E) ($n = 20$ worms; one-way ANOVA). (**H**) Schematic of nuclear acid binding motif (GXXG) in FUBL-3. (**I**) Representative images of DVE-1::GFP signal in *fubl-3(yth65)* mutants rescued with wild-type or GXXG-deficient FUBL-3 (ΔGXXG) in neuronal EGL-20 background. Scale bar, 100 μm. (**J**) Quantification of intestinal nuclei with DVE-1::GFP foci from (H) ($n = 20$ worms; one-way ANOVA). Error bars represent SEM. See also fig. S2.

UPR^{mt} activation. These results suggest that mitochondrial stress promotes both the expression and nuclear localization of FUBL-3.

Consistent with these observations, Western blot analyses using an antibody against endogenous FUBL-3 revealed a clear increase in protein abundance following prolonged mitochondrial stress (Fig. 2, C and D, and fig. S2, D to F). Notably, the accumulation of FUBL-3 was primarily observed in nuclear fractions, further supporting its nuclear accumulation under stress conditions. Collectively, these results demonstrate that mitochondrial perturbation leads to transcriptional up-regulation and nuclear accumulation of FUBL-3.

FUBL-3 functions in the nucleus to regulate the UPR^{mt}

The *C. elegans* gene *fubl-3* encodes a homolog of human FUBP1, a multifunctional nucleic acid–binding protein known to regulate transcription and RNA metabolism (*26*–*29*). Given that the activity of FUBP1 is closely linked to its subcellular localization, we first examined the spatial distribution of FUBL-3. Imaging of FUBL-3 translational reporter revealed that FUBL-3 localizes to both the nucleus and cytoplasm under basal conditions (Fig. 2A).

To determine whether its nuclear presence is required for UPR^{mt} regulation, we identified four potential nuclear localization signals (NLSs) in the FUBL-3 protein using the NLStradamus prediction tool (Fig. 2, E and F) (*30*). We then generated FUBL-3 variants lacking individual NLS motifs and expressed them in *fubl-3(yth65)* mutants carrying the DVE-1::GFP reporter under neuronal EGL-20 overexpression. Notably, the FUBL-3(ΔNLS1) mutant failed to localize to the nucleus and was unable to restore DVE-1::GFP nuclear accumulation in *fubl-3(yth65)* animals (Fig. 2, E to G, and fig. S2G). This result indicates that nuclear localization of FUBL-3 is essential for its role in UPR^{mt} induction.

FUBL-3 contains four KH domains, which are highly conserved nucleic acid–binding domains present in a wide range of prokaryotic and eukaryotic proteins (*31*, *32*). The defining feature of the KH domain is the GXXG motif, which forms part of the RNA/DNA binding cleft (*33*). To assess the importance of FUBL-3's nucleic acid–binding capacity, we mutated the conserved GXXG motif and expressed these mutant forms in *fubl-3(yth65)* animals. Strikingly, the nucleotide-binding defective FUBL-3 mutants failed to rescue DVE-1 nuclear accumulation or UPR^{mt} reporter activation (Fig. 2, H to J). Together, these results demonstrate that both nuclear localization and intact nucleic acid–binding activity are critical for FUBL-3 function in regulating the UPR^{mt}.

FUBL-3 coordinates mitochondrial stress–induced chromatin reorganization

Mitochondrial stress has been shown to induce chromatin reorganization in the intestinal nuclei of *C. elegans*. Specifically, RNAi-mediated knockdown of *cco-1* leads to smaller, more condensed nuclei in a DVE-1–dependent manner, a process that also requires components of the NuRD chromatin remodeling complex (*12*, *13*).

Given that FUBL-3 is essential for DVE-1 nuclear localization under mitochondrial stress, we hypothesized that FUBL-3 also plays a role in stress-induced chromatin reorganization. To test this, we examined chromatin structure and LIN-40/NuRD complex dynamics in *fubl-3(yth65)* mutant under basal and mitochondrial stress conditions (*cco-1* RNAi). Using a knock-in (KI) *dve-1::gfp* reporter, we confirmed that mitochondrial stress–induced DVE-1 nuclear accumulation was abolished in *fubl-3(yth65)* mutants (Fig. 3, A and B). We next assessed LIN-40::mCherry levels as a readout of NuRD complex recruitment. Under *cco-1* RNAi conditions, wild-type animals showed robust LIN-40::mCherry accumulation in intestinal nuclei, whereas *fubl-3(yth65)* mutants exhibited significantly reduced LIN-40 nuclear localization (Fig. 3, C and D).

To directly assess chromatin organization, we compared nuclear morphology between wild-type and *fubl-3(yth65)* animals. Under mitochondrial stress conditions, wild-type animals displayed marked chromatin condensation, whereas *fubl-3(yth65)* mutants retained enlarged, loosely packed nuclei (Fig. 3, E and F), indicating a failure to undergo chromatin compaction. These results indicate that FUBL-3 is essential for mitochondrial stress–induced chromatin reorganization in intestinal cells.

To test whether *dve-1* or *lin-40* act upstream of *fubl-3*, we examined *fubl-3* expression in animals treated with *dve-1* and *lin-40* RNAi. Neither the transcriptional up-regulation nor the nuclear accumulation of FUBL-3 protein in response to *cco-1* RNAi was affected in *dve-1* and *lin-40* RNAi treatment (fig. S3, A to H), suggesting that FUBL-3 acts upstream of these chromatin regulators.

To further assess the function of *fubl-3* in transcriptional regulation under mitochondrial stress, we performed RNA sequencing (RNA-seq) on wild-type and *fubl-3(yth65)* animals with or without *cco-1* RNAi. Among the 2011 genes significantly up-regulated in wild-type animals under mitochondrial stress ($|\mathrm{Log_2FC}| > 0$, adjusted $P < 0.05$), 616 genes were suppressed in *fubl-3* mutants ($\Delta\mathrm{Log_2FC} > 0.2$) (fig. S3I and data S1). Gene ontology (GO) analysis revealed enrichment in biological processes including "catabolic process," "transcription," "response to stress," and "defense response," further confirming that FUBL-3 is a key transcriptional regulator of mitochondrial stress adaptation (fig. S3J). Collectively, these findings position FUBL-3 upstream of DVE-1 and the NuRD complex, coordinating mitochondrial stress signals to chromatin reorganization and transcriptional activation of protective gene programs.

FUBP1 is a conserved regulator of mitochondrial stress–responsive chromatin remodeling in mammalian cells

To investigate the evolutionary conservation of FUBL-3–mediated UPR^{mt} regulation, we examined the function of its mammalian homolog, FUBP1. Expression of human FUBP1 in *C. elegans fubl-3(yth65)* mutants rescued DVE-1::GFP nuclear accumulation and restored UPR^{mt} activation (fig. S4, A and B), indicating functional conservation and enabling mechanistic dissection in mammalian systems.

To explore FUBP1's role in the mammalian UPR^{mt}, we first knocked down *FUBP1* in Hela cells and assessed the transcriptional response to mitochondrial proteotoxic stress induced by guanosine triphosphate phosphate (GTPP). FUBP1 depletion significantly attenuated the induction of key mitochondrial proteostasis genes, including *HSPA9*, *HSPD1*, *HSPE1*, and *LONP1* (Fig. 4, A and B and fig. S4C). Moreover, *FUBP1* transcription was specifically up-regulated in response to several mitochondrial stressors (GTPP, CCCP, and oligomycin), but not to ER stress (tunicamycin) or heat shock (Fig. 4, C and D and fig. S4D), mirroring the mitochondrial-specific responsiveness observed for *C. elegans* FUBL-3.

We next investigated whether FUBP1 regulates chromatin structure under mitochondrial stress. In U2OS cells, which exhibit well-defined nuclear architecture, GTPP treatment induced a robust nuclear accumulation of FUBP1, coinciding with increased chromatin condensation (Fig. 4, E and F). This stress-induced chromatin compaction was abolished upon *FUBP1* knockdown (Fig. 4, G and

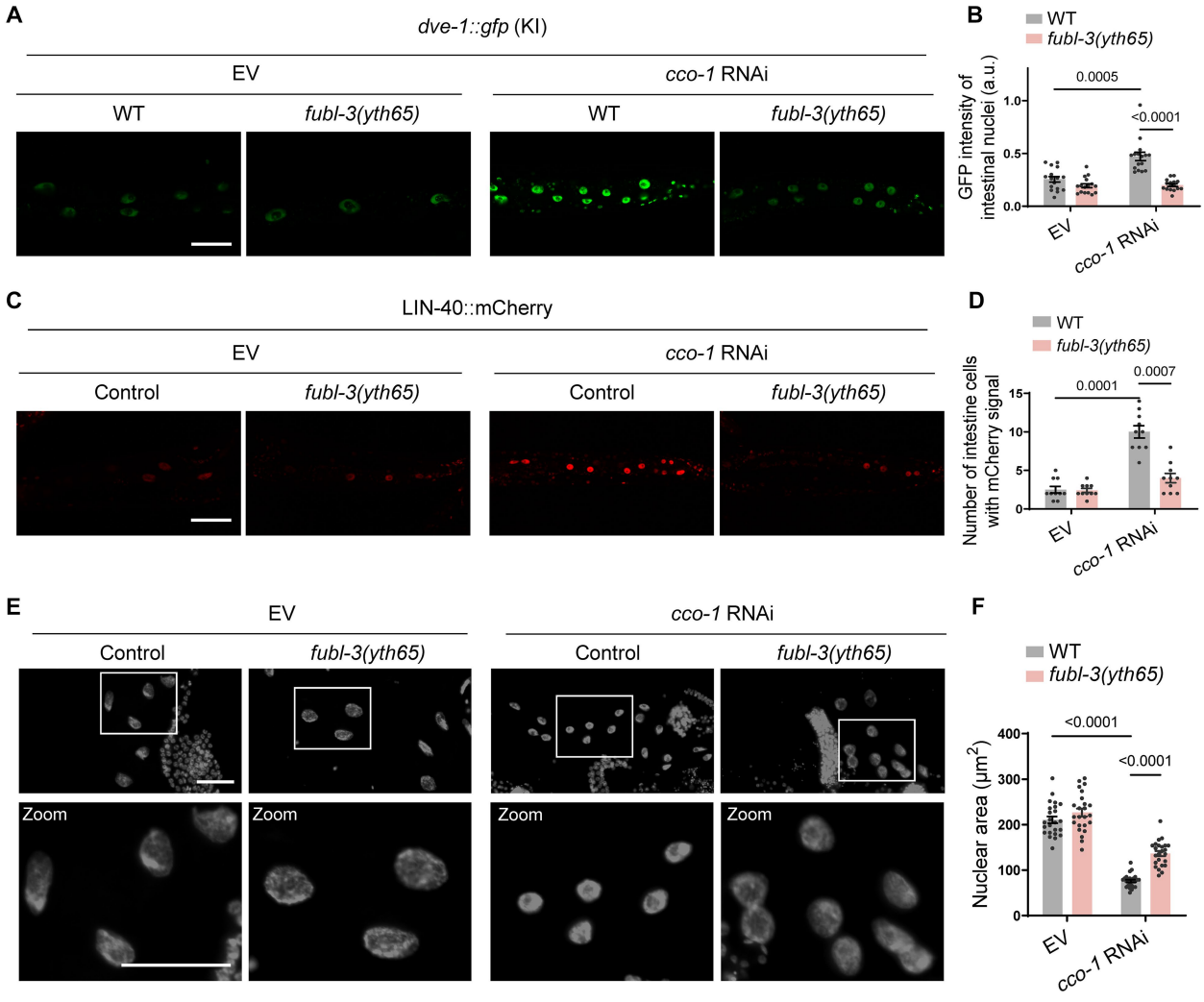

Fig. 3. FUBL-3 mediates NuRD-dependent chromatin compaction under mitochondrial stress. (**A**) Representative confocal images of *dve-1::gfp* (CRISPR KI) signal in day 1 adult *fubl-3(yth65)* mutants treated with EV or *cco-1* RNAi. (**B**) Quantification of nuclear GFP intensity in the intestine from (A) ($n = 16$ nuclei; two-way ANOVA). (**C**) Representative confocal images of LIN-40::mCherry signal in day 1 adult *fubl-3(yth65)* mutants treated with EV or *cco-1* RNAi. (**D**) Quantification of intestinal nuclei with strong LIN-40::mCherry signals from (C) ($n = 10$ worms; two-way ANOVA). (**E**) Representative maximal intensity projection images of DAPI-stained intestinal nuclei in day 1 adults of WT and *fubl-3(yth65)* mutants treated with EV or *cco-1* RNAi. DAPI (gray). The panels below show high-magnification views of boxed regions. (**F**) Quantification of the maximum cross-sectional area of intestinal nuclei from (E) ($n = 24$ nuclei; two-way ANOVA). Error bars represent SEM. Scale bar, 50 μm. See also fig. S3.

H and fig. S4, E and F), indicating a direct role for FUBP1 in chromatin remodeling response to mitochondrial dysfunction.

To define the genomic targets of FUBP1, we performed Cleavage Under Targets and Tagmentation (CUT&Tag) sequencing in U2OS cells. FUBP1 exhibited 24,871 high-confidence binding peaks under basal conditions, with nearly half (46.78%) located near transcriptional start sites (Fig. 4, I and J, and data S2). Motif enrichment analysis identified SP2- and NF-Y–binding motifs (fig. S4G), and many FUBP1-bound loci were associated with mitochondrial stress responses (e.g., *HSPD1* and *TOMM20*) and oncogenic pathways [e.g., the mechanistic target of rapamycin (mTOR) signaling and proteolysis], suggesting dual roles of FUBP1 in stress adaptation and cellular transformation (Fig. 4, K and L). Collectively, these results demonstrate that FUBP1 is a conserved nuclear effector of mitochondrial stress, orchestrating transcriptional activation and chromatin remodeling across species.

FUBL-3 overexpression preserves nuclear architecture and activates the UPR^{mt}

In wild-type animals, intestinal nuclei progressively lose chromatin integrity during aging, as evidenced by an increase in nuclear size and a decondensed structure (Fig. 5, A and B). Given the essential role of FUBL-3 in mitochondrial stress–induced chromatin remodeling, we examined whether FUBL-3 overexpression alone is sufficient to preserve nuclear architecture and activate the UPR^{mt}.

To this end, we generated transgenic strains expressing *fubl-3* under its endogenous promoter (FUBL-3 OE) or an intestine-specific promoter (*gly-19p*, gFUBL-3 OE). Intriguingly, both strains maintained compact, age-resistant chromatin organization in aged animals (Fig. 5, C and D), suggesting that FUBL-3 protects against age-related chromatin disintegration. As LIN-40/NuRD is a known chromatin remodeler and its mitochondrial stress–induced nuclear accumulation requires *fubl-3*, we hypothesized that the chromatin

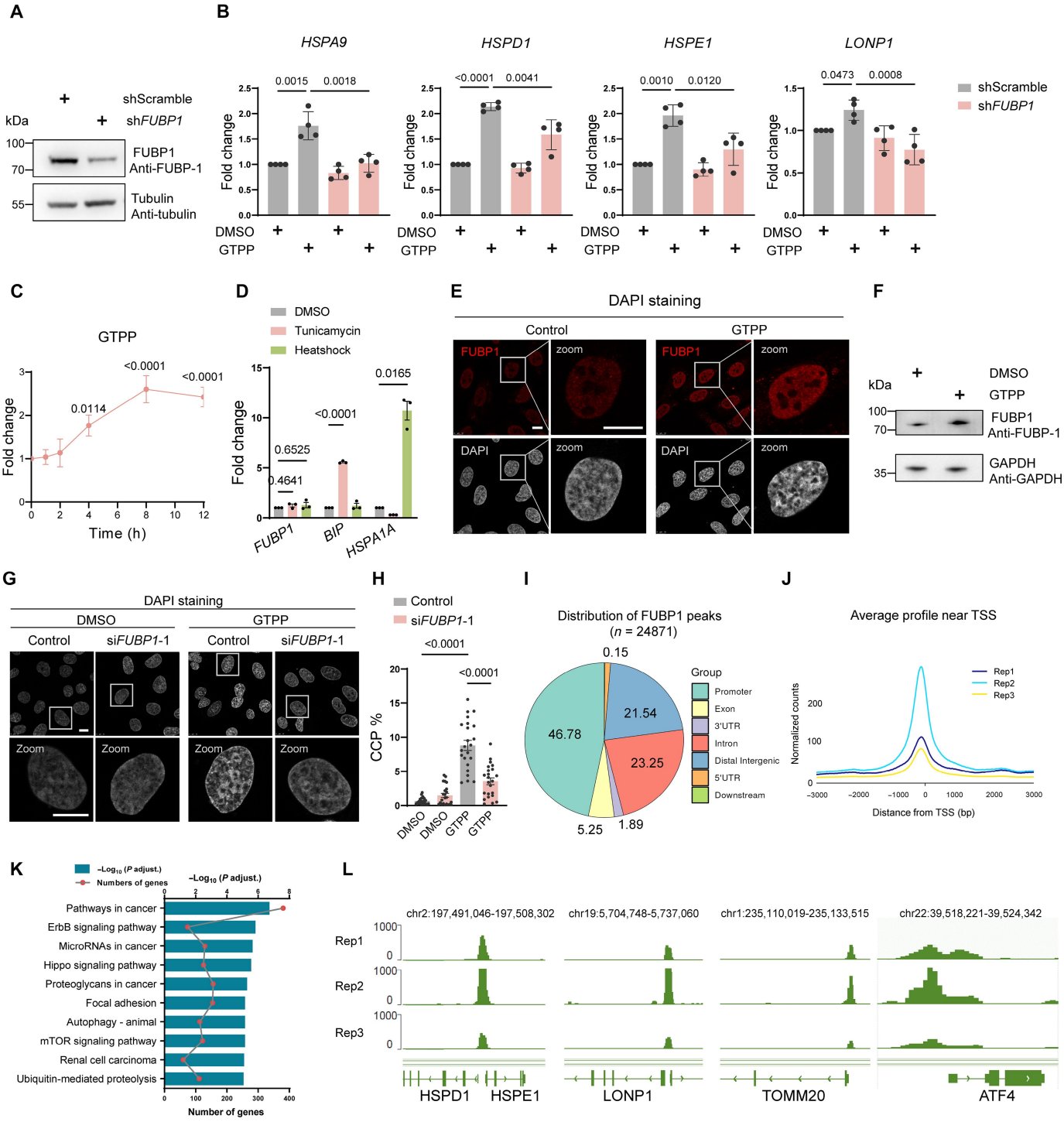

Fig. 4. Human FUBP1 regulates UPR^{mt} and chromatin remodeling. (**A**) Immunoblot of FUBP1 in HeLa cells assessing short hairpin RNA (shRNA) knockdown efficiency. (**B**) RT-qPCR analysis of *HSPA9*, *HSPD1*, *HSPE1*, and *LONP1* in HeLa cells stably transfected with shScramble or sh*FUBP1*, treated with dimethyl sulfoxide (DMSO) or 10 μM GTPP for 6 hours (h). ($n = 4$ replicates; two-way ANOVA). (**C**) Quantification of *FUBP1* mRNA levels in HeLa cells treated with 10 μM GTPP at the indicated time points. ($n = 3$ replicates; one-way ANOVA). (**D**) RT-qPCR analysis of *FUBP1*, *BIP*, and *HSPA1A* in HeLa cells treated with tunicamycin (2 μg/ml) for 6 hours or heat shock (42°C, 30 min). ($n = 3$ biological replicates; two-way ANOVA). (**E**) Confocal images of FUBP1 (red) and DAPI (gray) in U2OS cells treated with 10 μM GTPP for 8 hours. Scale bar, 10 μm. (**F**) Immunoblot analysis of FUBP1 in U2OS cells treated with 10 μM GTPP for 8 hours. (**G**) Confocal images of DAPI in U2OS cells transiently transfected with *FUBP1* small interfering RNAs, treated with DMSO or 10 μM GTPP for 8 hours. Scale bar, 10 μm. (**H**) Quantification of condensed chromatin percentage (CCP %) from (G) ($n = 23$ nuclei; two-way ANOVA). (**I**) Genomic annotation of FUBP1-bound accessible regions in U2OS cells. (**J**) Average profile aligned to TSSs from the three replications of FUBP1 CUT&Tag in U2OS cells. (**K**) GO-KEGG biological process analysis of FUBP1-bound genes. (**L**) Representative FUBP1 accessibility loci (e.g., *HSPD1*, *HSPE1*, *LONP1*, *TOMM20*, and *ATF4*) under CUT&Tag assay targeted by FUBP1. Error bars represent SEM. See also fig. S4.

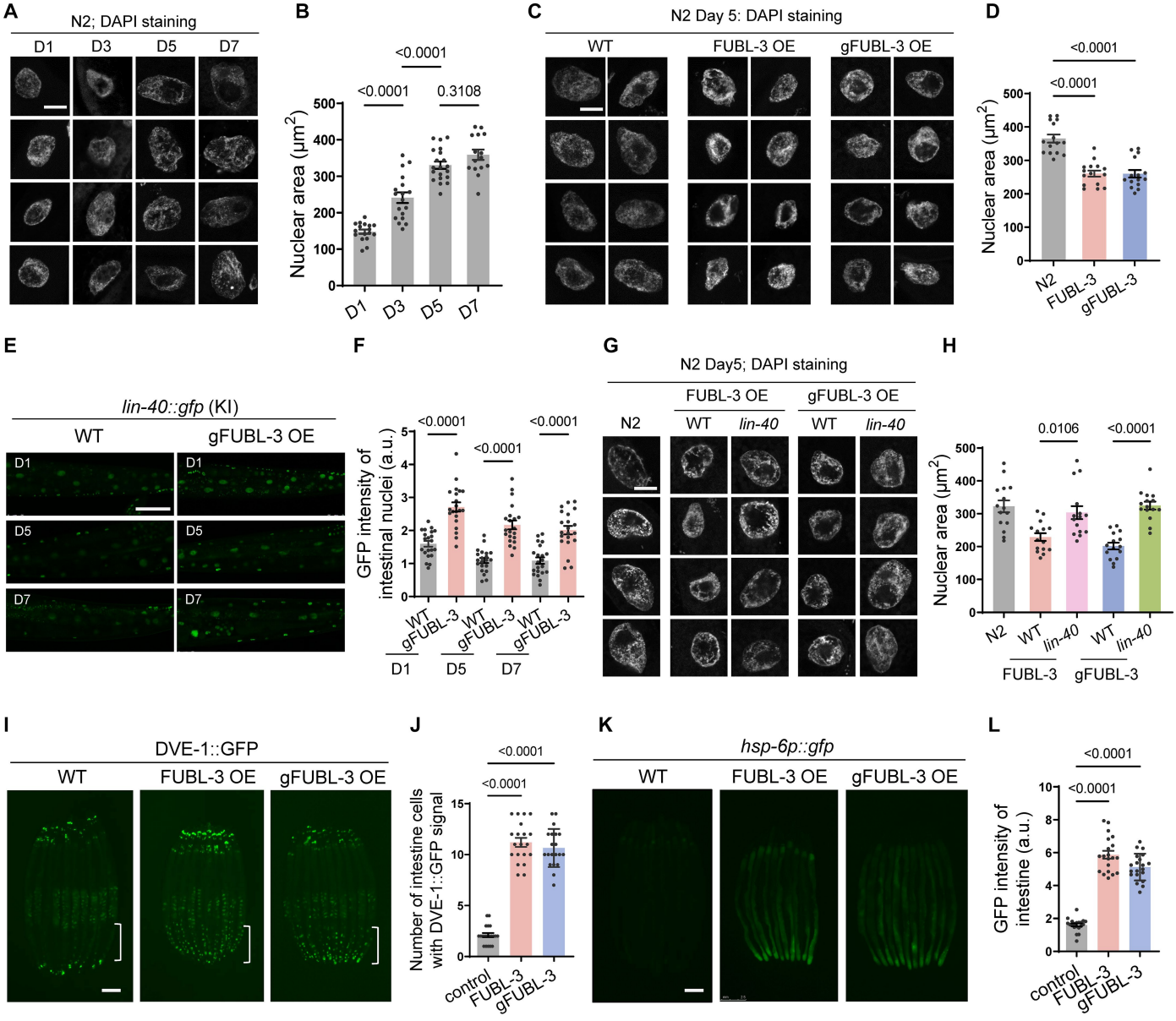

Fig. 5. FUBL-3 overexpression preserves nuclear architecture and induces UPR^{mt}. (**A**) DAPI-stained intestinal nuclei showing age-dependent decondensation in WT animals. DAPI (gray). Scale bar, 20 μm. (**B**) Quantification of the maximum cross-sectional area of intestinal nuclei from (A) ($n = 25$ nuclei; one-way ANOVA). (**C**) Representative maximal intensity projection images of DAPI-stained intestinal nuclei in day 7 adults in aged *fubl-3p::fubl-3* OE and *gly-19p::fubl-3* OE animals. DAPI (gray). Scale bar, 20 μm. (**D**) Quantification of chromatin compaction in aged FUBL-3 OE and gFUBL-3 OE animals from (C) ($n = 25$ nuclei; one-way ANOVA). (**E**) *lin-40::gfp* (CRISPR KI) signal in WT and *gly-19p::fubl-3* OE animals at indicated ages. Scale bar, 50 μm. (**F**) Quantification of GFP fluorescence intensity in intestinal nuclei from (E) ($n = 20$ nuclei; two-way ANOVA). (**G**) DAPI-stained intestinal nuclei in day 5 adults of FUBL-3 OE and gFUBL-3 OE animals with/without *lin-40(yth27)* mutation. DAPI (gray). Scale bar, 20 μm. (**H**) Quantification of the maximum cross-sectional area of intestinal nuclei from (G) ($n = 15$ nuclei; one-way ANOVA). (**I**) Representative images of DVE-1::GFP signals in day 1 adults of FUBL-3 OE and gFUBL-3 OE animals. Scale bar, 100 μm. (**J**) Quantification of intestinal nuclei with DVE-1::GFP foci from (I) ($n = 20$ worms; one-way ANOVA). (**K**) Representative images of *hsp-6p::gfp* induction in day 1 adults of FUBL-3 OE and gFUBL-3 OE animals. Scale bar, 100 μm. (**L**) Quantification of the intestinal GFP fluorescence intensity from (K) ($n = 20$ worms; one-way ANOVA). Error bars represent SEM. See also fig. S5.

protection conferred by FUBL-3 OE might be mediated through LIN-40/NuRD. We first examined endogenous LIN-40 protein levels in a *lin-40::gfp* CRISPR KI strain and found that gFUBL-3 OE maintained elevated LIN-40 levels on adult day 1, day 5, and day 7 (Fig. 5, E and F). Crucially, mutation of *lin-40* significantly suppressed the chromatin structural protection induced by gFUBL-3 OE during aging (Fig. 5, G and H). These results demonstrate that FUBL-3 is an upstream regulator of the LIN-40/NuRD chromatin remodeling complex to maintain chromatin architecture during aging.

Strikingly, FUBL-3 OE and gFUBL-3 OE animals also showed robust nuclear accumulation of DVE-1::GFP and activation of the *hsp-6p::gfp* UPR^{mt} reporter, even in the absence of exogenous mitochondrial stress (Fig. 5, I to L). Consistent with this, endogenous transcripts of canonical UPR^{mt} genes were significantly elevated in

both transgenic lines (fig. S5, E and F). This response was specific to the mitochondrial stress pathway: Neither the ER stress reporter (*hsp-4p::gfp*) nor the cytosolic heat shock reporter (*hsp-16.2p::gfp*) was activated by FUBL-3 overexpression (fig. S5, C and D). We next assessed whether FUBL-3-induced UPR^{mt} requires known pathway components. We demonstrate that FUBL-3 overexpression–induced UPR^{mt} activation requires not only the NuRD complex component LIN-40 and the transcription factor ATFS-1 and DVE-1 but also the H3K9me2 methyltransferase LIN-65/MET-2 and the H3K9me2 demethylase JMJD-1.2 (the *C. elegans* homolog of mammalian PHF-8) (fig. S5, G and H) (*12*–*15*).

Last, we observed that endogenous FUBL-3 protein level declined after day 3 (D3) of adulthood (fig. S5, A and B). This decline coincided with chromatin decondensation, suggesting that age-related loss of FUBL-3 may contribute to chromatin instability during the aging process.

FUBL-3 promotes mitochondrial stress–induced longevity and enhances multiple stress resistance

To determine the physiological relevance of FUBL-3-mediated chromatin remodeling and UPR^{mt} activation, we assessed its role in longevity and stress resistance. Under basal conditions, *fubl-3(yth65)* and *fubl-3(yth70)* mutants exhibited normal lifespan. However, both mutants strongly suppressed the lifespan extension induced by *cco-1* RNAi (Fig. 6A and fig. S6A). Furthermore, these mutants exhibited synthetic developmental delay when combined with *cco-1* RNAi (fig. S6B), suggesting that FUBL-3 is essential for coordinating growth and longevity in response to mitochondrial stress.

To assess whether FUBL-3 is sufficient to promote longevity, we overexpressed *fubl-3* ubiquitously (FUBL-3 OE) or in the intestine (gFUBL-3 OE). Both transgenes significantly extended median lifespan by 35 and 32%, respectively (Fig. 6B). By contrast, overexpression of FUBL-3 variants lacking nuclear localization (ΔNLS1) or nucleic acid–binding capacity (ΔGXXG) failed to confer longevity benefits (Fig. 6C), indicating that chromatin-targeted functions are required.

We next performed epistasis analysis to determine which downstream pathways mediate FUBL-3–induced longevity. RNAi knockdown of *lin-40* (NuRD complex) completely abolished the longevity benefit in both FUBL-3 OE and gFUBL-3 OE animals (Fig. 6, D and F), whereas *atfs-1* mutants only partially suppressed the lifespan extension (Fig. 6, D and F), indicating that chromatin remodeling is the primary driver, with mitochondrial retrograde signaling providing additional support.

Both FUBL-3 OE and gFUBL-3 OE animals exhibited normal development and brood size under standard conditions (fig. S6, C and D), except for a slight developmental delay in one FUBL-3 OE line. These results suggest that enhanced lifespan is not due to general developmental trade-offs.

Functionally, FUBL-3 OE animals exhibited enhanced resistance to acute oxidative stress (induced by paraquat) and heat shock (at 35°C) (Fig. 6, G and H), suggesting a systemic improvement in stress resilience. We further observed that FUBL-3 OE animals exhibited a modest but reproducible increase in oxidative stress reporter *gst-4p::gfp*, which was completely abolished in *skn-1(zj15)* mutants (fig. S6, E and F). This suggests that FUBL-3 overexpression mildly engages the SKN-1–mediated oxidative stress response pathway. To explore more molecular basis of this stress-resistant state, we performed RNA-seq in wild-type, FUBL-3 OE, and gFUBL-3 OE animals. A set of 327 shared up-regulated genes ($Log_2FC > 0$, adjusted $P < 0.05$) was enriched for GO analysis terms related to response to stress and "defense response to bacterium" (Fig. 6, I and J, and data S3). Consistently, both strains exhibited enhanced resistance to *Pseudomonas aeruginosa* (PA14) infection (Fig. 6K) (*34*), along with transcriptional activation of antimicrobial genes.

Last, genetic interaction analysis revealed that DAF-16/FOXO, a central effector of the insulin/insulin-like growth factor 1 pathway, was required for lifespan extension in both FUBL-3 OE and gFUBL-3 OE animals (fig. S6G), linking mitochondrial stress adaptation to conserved longevity pathways.

Together, these findings demonstrate that FUBL-3 functions as a key regulator of mitochondrial stress–induced chromatin remodeling, supporting transcriptional adaptation, increased stress resistance, and lifespan extension. Its capacity to maintain chromatin integrity, activate UPR^{mt}, and engage immune and aging pathways highlights its role in coordinating a multilayered antiaging response.

DISCUSSION

Our study identifies FUBL-3 in *C. elegans* and its mammalian homolog, FUBP1, as conserved regulators that convert mitochondrial stress into nuclear chromatin remodeling. In both systems, mitochondrial perturbation induces the nuclear accumulation of FUBL-3/FUBP1, which promotes NuRD- and DVE-1–dependent chromatin condensation and UPR^{mt} gene activation (Fig. 7). These findings support a model in which FUBL-3/FUBP1 functions as a mitochondrial stress sensor that safeguards nuclear architecture and transcriptional output, establishing a conserved axis of mitochondrial-nuclear communication. While our data clearly establish that mitochondrial stress promotes both the transcriptional up-regulation and nuclear accumulation of FUBL-3, the precise molecular sensors and signaling cascades linking organellar dysfunction to FUBL-3 activation remain to be elucidated. It is plausible that mitochondrial-derived metabolites or reactive oxygen species act as secondary messengers to trigger posttranslational modifications of FUBL-3, such as phosphorylation, acetylation, or ubiquitination, which may in turn regulate its nuclear import, stability, or affinity for chromatin partners. Future proteomic and genetic analyses will be essential to define the upstream factors that govern FUBL-3 dynamics in response to mitochondrial perturbation, thereby fully resolving this mitochondrial-to-nuclear signaling axis.

Chromatin integrity is essential for stress adaptation and healthy aging (*35*, *36*). Our findings show that FUBL-3 overexpression preserves chromatin compaction during aging and promotes longevity in an NuRD-dependent manner. Age-related decline in FUBL-3 expression may contribute to nuclear disorganization and impaired stress responses. FUBL-3–driven chromatin remodeling is accompanied by up-regulation of stress and immune response genes, highlighting a broader role in enhancing systemic resilience. These results position FUBL-3 as a key regulator that integrates mitochondrial proteostasis with chromatin-based transcriptional control, promoting longevity.

While FUBP1 is well known for its role in transcriptional regulation, RNA stability, and splicing (*37*, *38*), It binds to far-upstream sequence elements in promoters of key regulatory genes such as *c-MYC*, *USP29*, and *Cyclins* (*39*–*41*), and interacts with AU-rich elements in 3′ untranslated regions to modulate mRNA stability and translation (*42*, *43*). Functionally, FUBP1 has diverse roles in

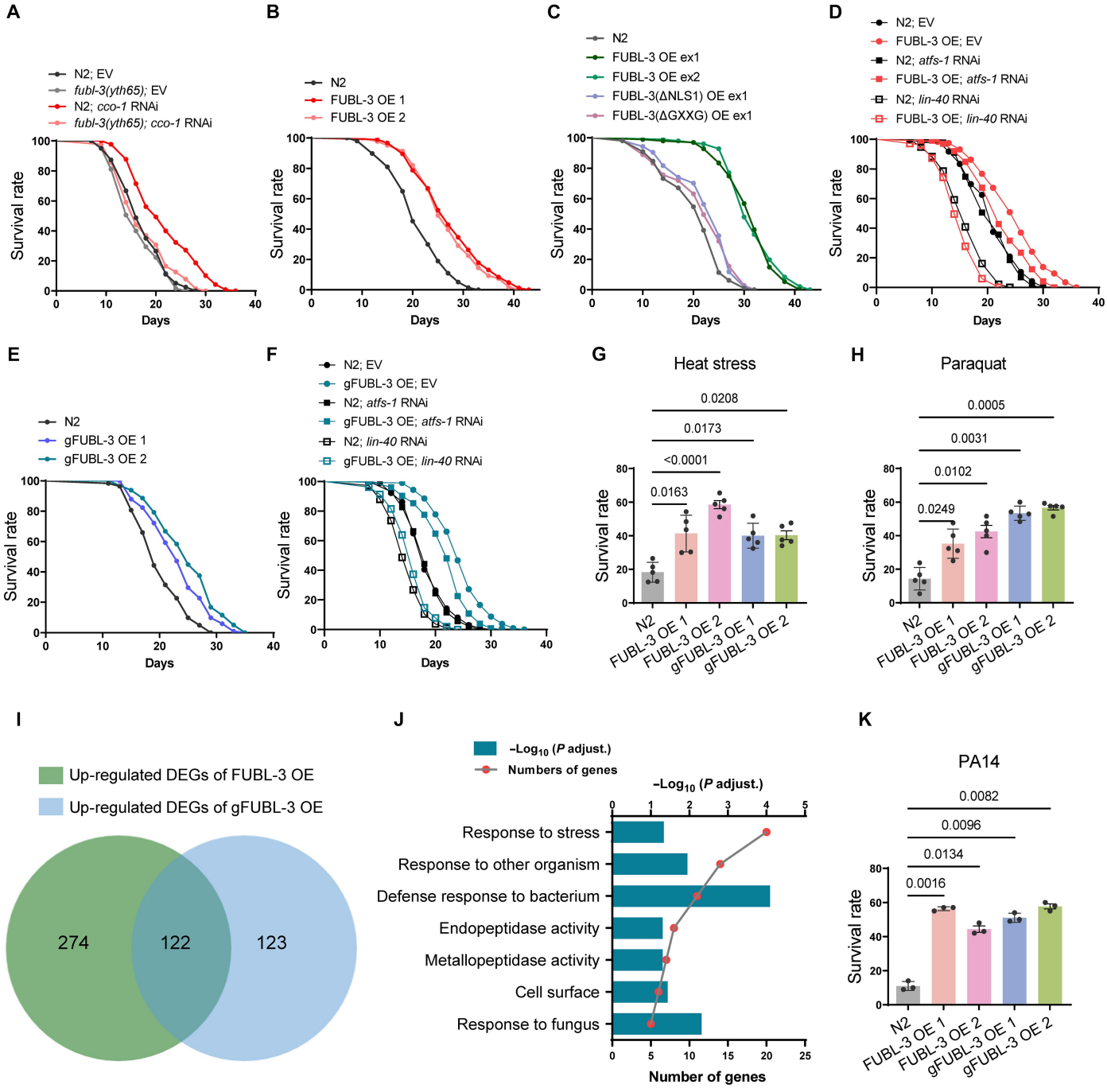

Fig. 6. FUBL-3 promotes longevity and multiple stress resistance. (**A**) Lifespan analysis of WT and *fubl-3(yth65)* animals treated with EV or *cco-1* RNAi. (**B**) Lifespan analysis of WT and two *fubl-3p::fubl-3* OE lines. (**C**) Lifespan analysis of WT animals, two *fubl-3p::fubl-3* OE lines (extrachromosomal array, ex), and animals overexpressing FUBL-3(ΔNLS1) or FUBL-3(ΔGXXG). (**D**) Lifespan analysis of WT and *fubl-3p::fubl-3* OE animals with *atfs-1* RNAi or *lin-40* RNAi. (**E**) Lifespan analysis of WT and two independent integrated *gly-19p::fubl-3* OE lines. (**F**) Lifespan analysis of WT and *gly-19p::fubl-3* OE animals with *atfs-1* RNAi or *lin-40* RNAi. (**G**) Survival rates of WT and OE lines (*fubl-3p::fubl-3*, *gly-19p::fubl-3*) after heat stress (6 hours at 35°C). (**H**) Survival rates of day 1 adult WT and OE lines (*fubl-3p::fubl-3*, *gly-19p::fubl-3*) after treatment with 100 mM paraquat for 90 mins. (**I**) Venn diagram displaying transcriptome overlap of up-regulated genes in *fubl-3p::fubl-3* and *gly-19p::fubl-3* OE animals. (**J**) GO–Encyclopedia of Genes and Genomes (KEGG) biological process analysis of overlapping up-regulated genes from (I). (**K**) Survival rates of WT and OE lines (*fubl-3p::fubl-3*, *gly-19p::fubl-3*) after 72 hours of exposure to *P. aeruginosa* (PA14) from the adult day 1 stage. *P* values: the log-rank test [(A) to (F)], one-way ANOVA [(G), (H), and (K)]. Error bars represent SEM. See also fig. S6.

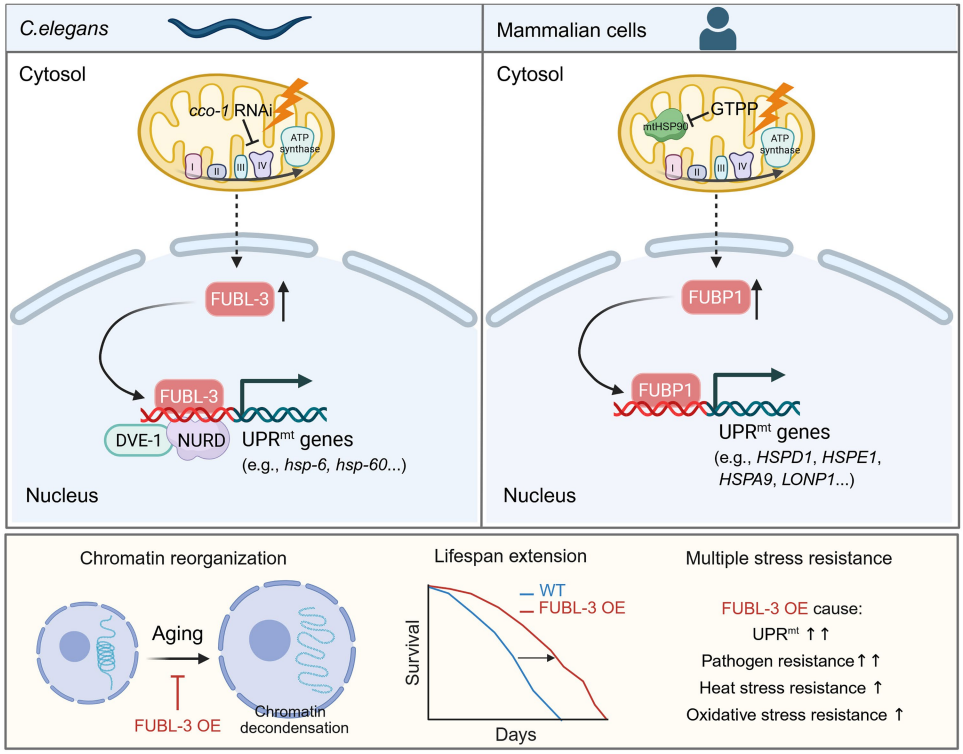

Fig. 7. FUBL-3/FUBP1 activates UPR^{mt} and induces chromatin compaction, leading to extended longevity. Schematic illustrating the conserved role of FUBL-3 in *C. elegans* and FUBP1 in mammalian cells. Both proteins respond to mitochondrial stress signals to promote UPR^{mt} gene expression and chromatin reorganization, ultimately leading to increased longevity and survival. Created in BioRender. Zhang, Q. (2025) https://BioRender.com/dxykwfl.

proliferation, apoptosis, migration, and tumor progression, and its context-dependent behavior in cancer has been well documented—acting as both a tumor suppressor and oncogene depending on cellular context (*44*–*46*).

Our study reveals an unexpected function of FUBP1 in cellular adaptation to mitochondrial stress. FUBP1 binds to stress-responsive loci, drives chromatin condensation, and activates UPR^{mt} genes—functions conserved from worms to humans. Its nuclear accumulation and promoter occupancy at proteostasis, autophagy, and mTOR-related genes suggest that FUBP1 coordinates stress responses with growth and survival pathways.

FUBP1's dual role in genome stability and proliferation necessitates a deeper understanding of its tissue-specific regulation. In proliferative contexts, FUBP1 can promote oncogenesis by regulating *c-MYC* and facilitating alternative splicing, whereas in differentiated tissues, it maintains genome stability through chromatin remodeling. Elucidating these context-specific functions—particularly its interaction with chromatin regulators such as NuRD—will be critical for understanding its therapeutic potential without triggering oncogenic programs.

Limitations and future directions

While we mapped FUBP1's chromatin occupancy, its direct transcriptional targets in UPR^{mt} remain to be validated. Identifying interacting partners that govern the functional activity of FUBP1 is, therefore, an interesting goal for further studies. In addition, the role of FUBL-3 in nonintestinal tissues (e.g., neurons) remains unexplored despite its systemic effects on longevity.

Concluding remarks

By bridging mitochondrial stress to chromatin dynamics and organismal physiology, FUBL-3/FUBP1 establishes a paradigm for inter-organelle communication. Our findings not only advance understanding of UPR^{mt} regulation but also highlight mitochondrial-nuclear cross-talk as a promising therapeutic target in aging and age-related diseases.

MATERIALS AND METHODS

C. elegans maintenance and strains

Studies were undertaken with *C. elegans* hermaphrodites. If needed, nematode males are obtained by heat shock. Nematodes were maintained and experimentally examined at 20°C on standard nematode growth medium (NGM) agar plates seeded with *Escherichia coli* OP50, unless otherwise indicated. Transgenic strains were generated by microinjection [transgene (50 ng/μl) + *rol-6*(pRF4) (50 ng/μl) coinjection marker] and integrated via ultraviolet irradiation. The *fubl-3* 2.3-kb promoter was used to generate *fubl-3p::mCherry*; *fubl-3* genomic DNA, which contains a mCherry tag without stop codon, were used to generate *fubl-3p::fubl-3::mCherry*. mCherry was from pBR322 backbone and ABclonal MultiF Seamless Assembly Mix was used for cloning. Strains used or generated are listed in the data S4.

EMS mutagenesis screen

Approximately 100 late-stage L4 worms were collected, washed three times with M9 buffer, and suspended in 3 ml of M9 buffer.

Separately, 20 μl of EMS (Sigma-Aldrich, #M-0880) was added to 1 ml of M9 buffer. The worm suspension (3 ml) was then combined with the EMS solution (1 ml), resulting in a final EMS concentration of 47 mM. The mixture was incubated at 20°C for 4 hours on a rotating platform. Following incubation, the worms were washed with M9 buffer and transferred to NGM plates. Healthy-appearing late L4 animals were selected as the parental generation (P0). The F1 progeny were allowed to self-fertilize, and the resulting F2 generation was screened for suppression of the DVE-1::GFP phenotype.

CRISPR-Cas9 mutagenesis in *C. elegans*

fubl-3 mutants (*yth70*, *yth71*) were generated using CRISPR-Cas9 (*47*). Single guide RNAs were designed to target exons (GGCATGCCAGCAGGAGTATA, GACGTTCGTTATTCGCGGCT). F1 progeny were screened by PCR/sequencing; homozygous lines were outcrossed six times.

Cell lines and culture conditions

All cells were cultured in a humidified incubator at 37°C with 5% CO_2. HeLa and HEK-293T cells were cultured with Dulbecco's modified Eagle's medium (Gibco) medium. U2OS cells were cultured with McCoy's 5A (modified) (Gibco) medium. All culture media were supplemented with 10% (v/v) fetal bovine serum (PAN) and 1% penicillin-streptomycin (Gibco). All cells were obtained from American Type Culture Collection. All cells were regularly tested for mycoplasma contamination, and cells used in experiments were negative for mycoplasma.

Generation of stable RNAi cell lines

Stable RNAi and stable overexpression cell lines were generated using lentiviral infections. To establish stable FUBP1 RNAi cell lines, primers for FUBP1 short hairpin RNA (shRNA) were designed following the manufacturer's instructions and cloned into the pLKO.1-Puro vector. The target sequence in FUBP1 is 5′- CGACTTGATGAAGATCTTAAT-3′ and 5′-GCTGAGTATTATAGACAACAA-3′. Three lentiviral particles for second-generation systems were generated according to the manufacturer's instructions. The plasmids as above were transfected into HEK-293T cells with a confluency of 90% for viral production. After 48 and 72 hours, cell medium that contained packaged lentivirus was collected and stored at −80°C. HeLa cells with a confluency of 60% then were infected with lentivirus produced by the corresponding shRNA vectors and selected with puromycin (5 μg/ml) for 24 hours after 12 hours of transduction. Expression of the FUBP1 was verified by immunoblotting.

RNAi in *C. elegans*

RNAi was performed using the feeding method. Synchronized worms at the L1 larval stage were placed onto NGM plates seeded with either HT115 *E. coli* harboring the empty vector L4440 (control) or bacteria expressing double-stranded RNA (dsRNA) targeting the gene of interest. Plates were supplemented with carbenicillin (100 μg/ml) and 1 mM isopropyl β-D-1-thiogalactopyranoside after autoclaving to induce dsRNA expression. Worms were maintained on the respective RNAi plates throughout development and experimentation unless otherwise specified. RNAi bacterial clones were sourced from the ORFeome-based Vidal RNAi library; clones unavailable in the Vidal library were obtained from the genomic Ahringer RNAi library.

RNAi of cell lines

To study the function of endogenous FUBP1, we attempted to generate U2OS FUBP1 KO cells using CRISPR however was unable to obtain homozygous knockout clones. Since previous studies described FUBP1 KO cell lines, we surmise the differences in cell type and culture conditions may have contributed to the differential viability. Instead, we used small interfering RNA (siRNA)–mediated RNAi to study the function of FUBP1.

The siRNA-mediated RNAi of FUBP1 in HeLa and U2OS cells was using jetPRIME transfection reagent. Cells were seeded into six-well plates at a density of ~2.5×10^5 cells per well. After 24 hours, cells with a confluency of 60 to 70% were transfected with 20 nM specific siRNAs or a nontargeting control according to the manufacturer's instructions. Cells were analyzed 72 hours after transfection by Western blotting or RT-qPCR for knockdown efficiency examination. The siRNA target sequence of FUBP1 is 5′-CAGGAUUAGUCAUUGGAAATT-3′ and 5′-GGUCAAGGCAACUGGAACATT-3′. Scramble and FUBP1 siRNA were synthesized by Guangzhou RiboBio Co. Ltd.

Drug treatment for cells

HeLa cells and U2OS cells were seeded into six-well plates at a density of ~2.5×10^5 cells per well. After 24 hours, the medium was replaced and cells were treated with dimethyl sulfoxide, 10 μM of GTPP for 8 hours or 10 μM CCCP, and 10 μM oligomycin A for different time points.

Lifespan analysis

Lifespan assays were p conducted at 20°C essentially as described (*48*). Synchronized young adult worms (day 0 of adulthood, defined as 24 hours post-L4 stage) were placed onto NGM plates seeded with *E. coli* OP50 (unless otherwise indicated). To prevent internal hatching (bagging), worms were transferred to plates supplemented with 5-fluoro-2′-deoxyuridine (final concentration 100 μM) upon reaching the late L4 stage and again on day 5 of adulthood. Viability was assessed every 48 hours by gentle prodding with a platinum wire; worms failing to respond were scored as dead. Animals that crawled off the plate, displayed extruded gonads, or died from bagging were censored. Survival curves were generated and statistical significance determined using the Log-rank (Mantel-Cox) test in GraphPad Prism 9.

Developmental rate analysis

Synchronized embryos (approximately 500 per strain) were placed onto NGM plates seeded with *E. coli* OP50 and incubated at 20°C. After 70 hours, the developmental stage (L1, L2, L3, L4, or adult) of all worms on each plate was recorded. The percentage of worms reaching adulthood was calculated.

Brood size analysis

Synchronized L4-stage hermaphrodites ($n = 10$ per strain) were individually transferred to fresh NGM plates seeded with *E. coli* OP50 at 20°C. Worms were transferred daily to new plates until egg-laying ceased. Progeny on each plate were counted 24 to 48 hours after parental removal to allow for hatching and development to L2/L3 stage. The total number of viable progeny per worm constituted the brood size. Assays were performed with at least three independent biological replicates. Data were analyzed using an unpaired, two-tailed Student's *t* test (assuming normal distribution and equal variance).

Pathogenesis analysis

Slow-killing assays were performed against *P. aeruginosa* strain PA14 as previously described (*5*) with minor modifications. Briefly, PA14 was cultured in King's B broth [tryptone (20 g/liter), K_2HPO_4 (1.5 g/liter), $MgSO_4$ (1.5 g/liter), and glycerol (10 ml/liter) (pH 7.2)] for 12 to 16 hours at 37°C with shaking. Bacterial cultures were then seeded onto modified slow-killing NGM plates (0.35% peptone) and dried overnight at room temperature. Plates were subsequently incubated at 37°C for 24 hours and equilibrated to 25°C before use. Synchronized young adult worms (Day 1 of adulthood) were washed extensively in M9 buffer to remove residual *E. coli* OP50 and transferred to PA14-seeded plates (approximately 30–40 worms per plate). Plates were maintained at 25°C. Survival was counted after 48 hours. Worms were scored as dead if unresponsive to repeated touch with a platinum pick. Animals found on the plate walls or exhibiting internal hatching were censored.

Paraquat killing analysis

Synchronized young adult worms (day 1 of adulthood) were exposed to oxidative stress by incubation in M9 buffer containing 100 mM paraquat (methyl viologen dichloride hydrate; Sigma-Aldrich, #36541) for 90 min at 20°C with gentle shaking. Following exposure, worms were washed twice in M9 buffer and transferred to recovery plates seeded with *E. coli* OP50. Survival was assessed after an 8-hour recovery period at 20°C. Worms unresponsive to touch were scored as dead. This assay was adapted as previously described (*49*).

Heatshock resistance analysis

Synchronized young adult worms (day 1 of adulthood) were subjected to heat stress by incubation at 34°C for 6 hours on NGM plates seeded with *E. coli* OP50. Following heat shock, worms were returned to 20°C and allowed to recover for 8 hours. Survival was assessed by touch response as described above.

Immunofluorescence staining of cell lines

Cells were seeded onto coverslips with a confluency of 60%. After treatment, the cells were washed once with prewarmed PBS and fixed immediately with prewarmed 4% paraformaldehyde at 37°C for 15 min. Then, the cells were permeabilized with 0.4% Triton X-100 for 5 min at room temperature. After incubation with 5% bovine serum albumin at room temperature for 1 hour, the cells were incubated with the primary antibody (1:500) overnight at 4°C. Following six washes with 0.05% Triton X-100 in PBS, the cells were incubated with Alexa488-, Alexa555-, or Alexa647-conjugated secondary antibody (1:1000) for 45 min at room temperature. After washing with 0.05% Triton X-100 in PBS for six times, the cells were mounted and subjected to observation.

Intestinal nuclear dissection, fixation, and morphometric analysis

Intestinal dissection and fixation were performed using modified protocols (*50*). Synchronized young adult worms were dissected in M9 buffer (22 mM KH_2PO_4, 42 mM Na_2HPO_4, 86 mM NaCl, and 1 mM $MgSO_4$) on poly-L-lysine–coated glass slides. Dissected intestines were immediately fixed in ice-cold methanol for 10 min, followed by ice-cold acetone for 10 min at −20°C. Slides were then rehydrated in phosphate-buffered saline [PBS; 137 mM NaCl, 2.7 mM KCl, 10 mM Na_2HPO_4, and 1.8 mM KH_2PO_4 (pH 7.4)] and washed three times (5 min each) in fresh PBS. Nuclei were counterstained by mounting slides with Vectashield Antifade Mounting Medium containing DAPI (4′,6-diamidino-2-phenylindole; Vector Laboratories, H-1200). Fixed intestinal samples were imaged using a Leica TCS SP8 laser scanning confocal microscope equipped with a 63×/1.40 numerical aperture oil immersion objective. Z stacks (0.5-μm step size) encompassing the entire intestinal depth were acquired using LAS X software (Leica Microsystems). Nuclear cross-sectional area quantification was performed in ImageJ (National Institutes of Health): Maximum-intensity projections of Z stacks were generated, individual intestinal nuclei were manually segmented based on DAPI fluorescence, and the maximum cross-sectional area (micrometer square) for each nucleus was extracted using the "Analyze Particles" function with thresholding.

Microscopy and image acquisition

Whole-worm bright-field imaging

Live worms were anesthetized in 50 mM sodium azide (NaN_3) on 2% agarose pads. Images were acquired using a Leica M165 FC stereo microscope controlled by LAS X software. Exposure times were kept constant within each experimental set.

Confocal microscopy

Immunostained samples or transgenic reporters were imaged using a Leica TCS SP8 confocal microscope with appropriate laser lines and filter sets. All presented images are representative of at least three independent biological replicates, with multiple fields of view per replicate.

Immunoblotting analysis

Cell lysates

Adherent cells were washed twice with ice-cold PBS and lysed directly on the plate using ice-cold radioimmunoprecipitation assay buffer [50 mM tris-HCl (pH 8.0), 150 mM NaCl, 1% NP-40, 0.5% sodium deoxycholate, and 0.1% SDS]) supplemented with 1× EDTA-free protease inhibitor cocktail (Roche, 04693159001) and 1 mM phenylmethylsulfonyl fluoride. Lysates were clarified by centrifugation at 16,000*g* for 15 min at 4°C. Protein concentration was determined by BCA assay (Pierce). Lysates were diluted in 5× Laemmli SDS–polyacrylamide gel electrophoresis (SDS-PAGE) sample buffer [250 mM tris-HCl (pH 6.8), 10% SDS, 50% glycerol, 0.02% bromophenol blue, and 5% β-mercaptoethanol] and denatured at 95°C for 10 min.

C. elegans lysates

Synchronized young adult worms (approximately 100 per sample) were washed in M9 buffer, pelleted, and snap-frozen in liquid nitrogen. Frozen pellets were resuspended in 1x SDS-PAGE sample buffer at a ratio of ~10 worm/μL, vortexed vigorously, and immediately boiled at 95°C for 15 min. Samples were briefly centrifuged to pellet debris.

Electrophoresis and immunodetection

Protein samples were resolved by SDS-PAGE on 8 to 15% tris-glycine gels (Bio-Rad) and electrotransferred to nitrocellulose membranes (0.45-μm pore size; Bio-Rad) using a Trans-Blot Turbo transfer system (Bio-Rad). Membranes were blocked for 1 hour at room temperature in NcmBlot Blocking Buffer (NCM Biotech, P30500) or 5% nonfat dry milk in TBST (tris-buffered saline with 0.1% Tween-20). Primary antibodies were diluted in blocking buffer and incubated overnight at 4°C. After three washes (10 min each) in TBST, membranes were incubated with appropriate horseradish peroxidase–conjugated secondary antibodies (1:5000 to 1:10000 dilution in

blocking buffer) for 1 hour at room temperature. Following three TBST washes, immunoreactive bands were visualized using enhanced chemiluminescence substrate (Tanon) and detected on a Tanon 5200 Multi Chemiluminescent Imaging System. Primary antibody details (catalog numbers and dilutions) are provided in data S4.

RNA extraction and RT-qPCR

Synchronized worms at the early L4 larval stage were collected in M9 buffer and snap-frozen in liquid nitrogen. Total RNA was extracted using TRIzol X-100 reagent (Invitrogen, 15596026) according to the manufacturer's instructions. Briefly, frozen worm pellets were homogenized in 500 μl of TRIzol X-100 by repeated freeze-thaw cycles (liquid nitrogen/37°C water bath, three cycles). Following chloroform phase separation, RNA was precipitated with isopropanol, washed with 75% ethanol, and dissolved in nuclease-free water. gDNA contamination was removed by treatment with RQ1 Ribonuclease-free deoxyribonuclease (DNase) (Promega, M6101) at 37°C for 30 min. DNase was inactivated by adding Stop Solution and heating (65°C for 10 min). RNA was repurified using phenol-chloroform extraction and ethanol precipitation. RNA concentration and purity (A260/A280 > 1.8) were determined spectrophotometrically (NanoDrop). Total RNAs of cultured cell lines were extracted using the FastPure Cell/Tissue Total RNA Isolation kit V2 (Vazyme) following the manufacturer's instructions. First-strand cDNA synthesis was performed from 1 μg total RNA using the M-MLV Reverse Transcriptase kit (Thermo Fisher Scientific, 28025013) with oligo$(dT)_{18}$ primers, according to the manufacturer's protocol.

qPCR was performed using SYBR Green Real-time PCR Master Mix (TOYOBO, QPK-201) on a CFX96 Touch Real-Time PCR Detection System (Bio-Rad). Reactions (10 μl of the final volume) contained 1× Master Mix, 200 nM gene-specific primers (sequences in data S4), and diluted cDNA template (equivalent to ~10 ng of input RNA). Cycling conditions were: 95°C for 1 min; 40 cycles of 95°C for 15 s, 60°C for 30 s, 72°C for 30 s; followed by a melt curve analysis (65° to 95°C, increment 0.5°C/5 s). Relative mRNA expression levels were calculated using the comparative ΔΔCt method, with *act-3* (actin) serving as the endogenous reference gene. Data normalization was performed within each biological replicate. Each experiment included at least three independent biological replicates, each analyzed with technical triplicates.

RNA-seq analysis

A total of 2×10^5 in vitro–cultured U2OS cells were collected in TRIzol buffer. For RNA-seq analysis, libraries were prepared using NEBNext Ultra II RNA Library Prep Kit and then sequenced on Illumina NovaSeq 6000 platform. Raw reads were filtered using Cutadapt (v1.15) and aligned with the GRCm39 genome using HISAT2 v2.0.5. Read count values on each gene were compared using HTSeq (v0.9.1) and normalized to fragments per kilobase of transcript per million mapped reads (FPKM). Then, difference expression of genes was analyzed using DESeq (v1.30.0) (fold change ≥1.2 and $P < 0.05$). GO enrichment analysis of the different expressed genes was performed using Database for Annotation, Visualization, and Integrated Discovery. The enrichment analysis of the KEGG pathway of differential genes was performed using https://www.genome.jp/kegg/ ($P < 0.05$).

CUT&Tag assay

A total of 5×10^5 in vitro–cultured U2OS cells were collected for the preparation of CUT&Tag-seq libraries. In brief, cells collected from culture were washed and counted, then nuclei were collected. Once bound to ConA magnetic beads and permeabilization, nuclei were incubated with primary antibody overnight at 4°C. Beads were washed, followed by incubation with pA-Tn5 (S603-02, Vazyme Biotech Co. Ltd) at room temperature for 1 hour followed by Mg^{2+}-triggered tagmentation. Fragmented DNA was isolated using phenol-chloroform-isoamyl alcohol, and the final sequencing library was amplified using i5 and i7 indexed primers. CUT&Tag sequencing was performed by Personal Biotechnology Company (Shanghai, China) by using the Illumina Novaseq platform.

Quantification of chromatin condensation level using ImageJ

Chromatin condensation level was quantified in DAPI-stained nuclei using ImageJ (version 1.53) through an edge-based analysis protocol, which is adjusted from previously described (*51*). Briefly, nuclei images were preprocessed by converting to 8-bit grayscale and reducing pixel resolution by a factor of 4 to minimize noise sensitivity. Sobel edge detection (Process > Filters > Sobel) was applied to highlight intensity gradients corresponding to chromatin boundaries. The resulting edge map was thresholded (fixed threshold: 100 to 255) to isolate significant edges (Image > Adjust > Threshold), followed by skeletonization to refine edges to single-pixel width (Process > Binary > Skeletonize). Nuclear outlines were excluded by eroding the nuclear mask by 1 pixel (Process > Binary > Erode), and edge pixels within the eroded region were counted using Analyze > Analyze Particles (size: 0–Infinity). The chromatin condensation parameter (CCP) was calculated as the ratio of edge pixels to nuclear area, expressed as a percentage [CCP% = (edge pixels/nuclear area) × 100]. This method ensures high reproducibility and aligns with visual assessments of chromatin organization.

Statistical analysis and reproducibility

Experimental data were analyzed using GraphPad Prism (version 9). For all graphs, the error bars indicate the means ± SEM, differences were considered significant when $P < 0.05$, and P values are marked in the figure. n represents number of biological replicates unless otherwise indicated, and no data were excluded from the analyses. To compare two normally distributed groups, two-tailed t tests were used. For comparisons between multiple groups with one fixed factor, an ordinary one-way analysis of variance (ANOVA) or repeated measures (RM) one-way ANOVA was used, followed by Dunnett's multiple comparisons test or Tukey's multiple comparisons test. For comparison between multiple groups with two fixed factors, an ordinary two-way ANOVA or RM two-way ANOVA was used, Sidak's multiple comparisons test. The homogeneity of variances was tested using F test. Lifespans and slow-killing assays were analyzed using Mantel-Cox log-rank test. All experiments were performed at least three times yielding similar results and comprised of biological replicates.

Supplementary Materials

The PDF file includes:

Figs. S1 to S6

Legends for data S1 to S5

Other Supplementary Material for this manuscript includes the following:

Data S1 to S5

REFERENCES

1. A. Mottis, S. Herzig, J. Auwerx, Mitocellular communication: Shaping health and disease. *Science* **366**, 827–832 (2019).
2. Q. Zhao, J. Wang, I. V. Levichkin, S. Stasinopoulos, M. T. Ryan, N. J. Hoogenraad, A mitochondrial specific stress response in mammalian cells. *EMBO J.* **21**, 4411–4419 (2002).
3. C. M. Haynes, K. Petrova, C. Benedetti, Y. Yang, D. Ron, ClpP mediates activation of a mitochondrial unfolded protein response in *C. elegans*. *Dev. Cell* **13**, 467–480 (2007).
4. O. Matilainen, P. M. Quirós, J. Auwerx, Mitochondria and epigenetics – Crosstalk in homeostasis and stress. *Trends Cell Biol.* **27**, 453–463 (2017).
5. M. W. Pellegrino, A. M. Nargund, N. V. Kirienko, R. Gillis, C. J. Fiorese, C. M. Haynes, Mitochondrial UPR-regulated innate immunity provides resistance to pathogen infection. *Nature* **516**, 414–417 (2014).
6. J. Feng, F. Bussière, S. Hekimi, Mitochondrial electron transport is a key determinant of life span in *Caenorhabditis elegans*. *Dev. Cell* **1**, 633–644 (2001).
7. X. Liu, N. Jiang, B. Hughes, E. Bigras, E. Shoubridge, S. Hekimi, Evolutionary conservation of the clk-1-dependent mechanism of longevity: Loss of mclk1 increases cellular fitness and lifespan in mice. *Genes Dev.* **19**, 2424–2434 (2005).
8. J. M. Copeland, J. Cho, T. Lo, J. H. Hur, S. Bahadorani, T. Arabyan, J. Rabie, J. Soh, D. W. Walker, Extension of *Drosophila* life span by RNAi of the mitochondrial respiratory chain. *Curr. Biol.* **19**, 1591–1598 (2009).
9. N. S. Chandel, Evolution of mitochondria as signaling organelles. *Cell Metab.* **22**, 204–206 (2015).
10. T. Shpilka, C. M. Haynes, The mitochondrial UPR: Mechanisms, physiological functions and implications in ageing. *Nat. Rev. Mol. Cell Biol.* **19**, 109–120 (2018).
11. D. Zhu, X. Li, Y. Tian, Mitochondrial-to-nuclear communication in aging: An epigenetic perspective. *Trends Biochem. Sci.* **47**, 645–659 (2022).
12. Y. Tian, G. Garcia, Q. Bian, K. K. Steffen, L. Joe, S. Wolff, B. J. Meyer, A. Dillin, Mitochondrial stress induces chromatin reorganization to promote longevity and UPRmt. *Cell* **165**, 1197–1208 (2016).
13. D. Zhu, X. Wu, J. Zhou, X. Li, X. Huang, J. Li, J. Wu, Q. Bian, Y. Wang, Y. Tian, NuRD mediates mitochondrial stress–induced longevity via chromatin remodeling in response to acetyl-CoA level. *Sci. Adv.* **6**, eabb2529 (2020).
14. C. Merkwirth, V. Jovaisaite, J. Durieux, O. Matilainen, S. D. Jordan, P. M. Quiros, K. K. Steffen, E. G. Williams, L. Mouchiroud, S. U. Tronnes, V. Murillo, S. C. Wolff, R. J. Shaw, J. Auwerx, A. Dillin, Two conserved histone demethylases regulate mitochondrial stress-induced longevity. *Cell* **165**, 1209–1223 (2016).
15. T. Y. Li, M. B. Sleiman, H. Li, A. W. Gao, A. Mottis, A. M. Bachmann, G. El Alam, X. Li, L. J. E. Goeminne, K. Schoonjans, J. Auwerx, The transcriptional coactivator CBP/p300 is an evolutionarily conserved node that promotes longevity in response to mitochondrial stress. *Nat. Aging* **1**, 165–178 (2021).
16. C. Benedetti, C. M. Haynes, Y. Yang, H. P. Harding, D. Ron, Ubiquitin-like protein 5 positively regulates chaperone gene expression in the mitochondrial unfolded protein response. *Genetics* **174**, 229–239 (2006).
17. C. M. Haynes, Y. Yang, S. P. Blais, T. A. Neubert, D. Ron, The matrix peptide exporter HAF-1 signals a mitochondrial UPR by activating the transcription factor ZC376.7 in *C. elegans*. *Mol. Cell* **37**, 529–540 (2010).
18. J. Durieux, S. Wolff, A. Dillin, The cell-non-autonomous nature of electron transport chain-mediated longevity. *Cell* **144**, 79–91 (2011).
19. Q. Zhang, X. Wu, P. Chen, L. Liu, N. Xin, Y. Tian, A. Dillin, The mitochondrial unfolded protein response is mediated cell-non-autonomously by retromer-dependent Wnt signaling. *Cell* **174**, 870–883.e17 (2018).
20. K. M. Berendzen, J. Durieux, L. W. Shao, Y. Tian, H.-e. Kim, S. Wolff, Y. Liu, A. Dillin, Neuroendocrine coordination of mitochondrial stress signaling and proteostasis. *Cell* **166**, 1553–1563.e10 (2016).
21. L. W. Shao, R. Niu, Y. Liu, Neuropeptide signals cell non-autonomous mitochondrial unfolded protein response. *Cell Res.* **26**, 1182–1196 (2016).
22. L. T. Chen, C. T. Lin, L. Y. Lin, J. M. Hsu, Y. C. Wu, C. L. Pan, Neuronal mitochondrial dynamics coordinate systemic mitochondrial morphology and stress response to confer pathogen resistance in *C. elegans*. *Dev. Cell* **56**, 1770–1785.e12 (2021).
23. J. Li, J. Cui, Y. Tian, Neuron-periphery mitochondrial stress communication in aging and diseases. *Life Med.* **1**, 168–178 (2022).
24. Y. Liu, J. Zhou, N. Zhang, X. Wu, Q. Zhang, W. Zhang, X. Li, Y. Tian, Two sensory neurons coordinate the systemic mitochondrial stress response via GPCR signaling in *C. elegans*. *Dev. Cell* **57**, 2469–2482.e5 (2022).
25. J. Li, J. Cui, X. Li, D. Zhu, Z. Chen, X. Huang, Y. Wang, Q. Wu, Y. Tian, TMBIM-2 orchestrates systemic mitochondrial stress response via facilitating Ca^{2+} oscillations. *J. Cell Biol.* **224**, e202408050 (2025).
26. L. Debaize, M. B. Troadec, The master regulator FUBP1: Its emerging role in normal cell function and malignant development. *Cell. Mol. Life Sci.* **76**, 259–281 (2019).
27. J. Miro, A. M. Laaref, V. Rofidal, R. Lagrafeuille, S. Hem, D. Thorel, D. Mechin, K. Mamchaoui, V. Mouly, M. Claustres, S. Tuffery-Giraud, FUBP1: A new protagonist in splicing regulation of the DMD gene. *Nucleic Acids Res.* **43**, 2378–2389 (2015).
28. S. Ebersberger, C. Hipp, M. M. Mulorz, A. Buchbender, D. Hubrich, H. S. Kang, S. Martínez-Lumbreras, P. Kristofori, F. X. R. Sutandy, L. Llacsahuanga Allcca, J. Schönfeld, C. Bakisoglu, A. Busch, H. Hänel, K. Tretow, M. Welzel, A. Di Liddo, M. M. Möckel, K. Zarnack, I. Ebersberger, S. Legewie, K. Luck, M. Sattler, J. König, FUBP1 is a general splicing factor facilitating 3′ splice site recognition and splicing of long introns. *Mol. Cell* **83**, 2653–2672.e15 (2023).
29. U. Rabenhorst, F. B. Thalheimer, K. Gerlach, M. Kijonka, S. Böhm, D. S. Krause, F. Vauti, H. H. Arnold, T. Schroeder, F. Schnütgen, H. von Melchner, M. A. Rieger, M. Zörnig, Single-stranded DNA-binding transcriptional regulator FUBP1 is essential for fetal and adult hematopoietic stem cell self-renewal. *Cell Rep.* **11**, 1847–1855 (2015).
30. A. N. Nguyen Ba, A. Pogoutse, N. Provart, A. M. Moses, NLStradamus: A simple hidden Markov model for nuclear localization signal prediction. *BMC Bioinformatics* **10**, 202 (2009).
31. R. Valverde, L. Edwards, L. Regan, Structure and function of KH domains. *FEBS J.* **275**, 2712–2726 (2008).
32. X. Ni, S. Knapp, A. Chaikuad, Comparative structural analyses and nucleotide-binding characterization of the four KH domains of FUBP1. *Sci. Rep.* **10**, 1–10 (2020).
33. M. Barnes, G. Van Rensburg, W. M. Li, K. Mehmood, S. Mackedenski, C. M. Chan, D. T. King, A. L. Miller, C. H. Lee, Molecular insights into the coding region determinant-binding protein-RNA interaction through site-directed mutagenesis in the heterogeneous nuclear Ribonucleoprotein-K-homology domains. *J. Biol. Chem.* **290**, 625–639 (2015).
34. N. V. Kirienko, B. O. Cezairliyan, F. M. Ausubel, J. R. Powell, Pseudomonas aeruginosa PA14 pathogenesis in *Caenorhabditis elegans*. *Methods Mol. Biol.* **1149**, 653–669 (2014).
35. J. Feser, J. Tyler, Chromatin structure as a mediator of aging. *FEBS Lett.* **585**, 2041–2048 (2011).
36. G. Pegoraro, N. Kubben, U. Wickert, H. Göhler, K. Hoffmann, T. Misteli, Ageing-related chromatin defects through loss of the NURD complex. *Nat. Cell Biol.* **11**, 1261–1267 (2009).
37. D. T. Braddock, J. M. Louis, J. L. Baber, D. Levens, G. M. Clore, Structure and dynamics of KH domains from FBP bound to single-stranded DNA. *Nature* **415**, 1051–1056 (2002).
38. J. Samarin, V. Laketa, M. Malz, S. Roessler, I. Stein, E. Horwitz, S. Singer, E. Dimou, A. Cigliano, M. Bissinger, C. S. Falk, X. Chen, S. Dooley, E. Pikarsky, D. F. Calvisi, C. Schultz, P. Schirmacher, K. Breuhahn, PI3K/AKT/mTOR-dependent stabilization of oncogenic far-upstream element binding proteins in hepatocellular carcinoma cells. *Hepatology* **63**, 813–826 (2016).
39. J. Liu, F. Kouzine, Z. Nie, H. J. Chung, Z. Elisha-Feil, A. Weber, K. Zhao, D. Levens, The FUSE/FBP/FIR/TFIIH system is a molecular machine programming a pulse of c-myc expression. *EMBO J.* **25**, 2119–2130 (2006).
40. R. Duncan, L. Bazar, G. Michelotti, T. Tomonaga, H. Krutzsch, M. Avigan, D. Levens, A sequence-specific, single-strand binding protein activates the far upstream element of c-myc and defines a new DNA-binding motif. *Genes Dev.* **8**, 465–480 (1994).
41. J. S. Elman, T. K. Ni, K. E. Mengwasser, D. Jin, A. Wronski, S. J. Elledge, C. Kuperwasser, Identification of FUBP1 as a long tail cancer driver and widespread regulator of tumor suppressor and oncogene alternative splicing. *Cell Rep.* **28**, 3435–3449.e5 (2019).
42. N. Irwin, V. Baekelandt, L. Goritchenko, L. I. Benowitz, Identification of two proteins that bind to a pyrimidine-rich sequence in the 3′-untranslated region of GAP-43 mRNA. *Nucleic Acids Res.* **25**, 1281–1288 (1997).
43. M. E. Olanich, B. L. Moss, D. Piwnica-Worms, R. R. Townsend, J. D. Weber, Identification of FUSE-binding protein 1 as a regulatory mRNA-binding protein that represses nucleophosmin translation. *Oncogene* **30**, 77–86 (2011).
44. M. Malz, A. Weber, S. Singer, V. Riehmer, M. Bissinger, M. O. Riener, T. Longerich, C. Soll, A. Vogel, P. Angel, P. Schirmacher, K. Breuhahn, Overexpression of far upstream element binding proteins: A mechanism regulating proliferation and migration in liver cancer cells. *Hepatology* **50**, 1130–1139 (2009).
45. J. Duan, X. Bao, X. Ma, Y. Zhang, D. Ni, H. Wang, F. Zhang, Q. Du, Y. Fan, J. Chen, S. Wu, X. Li, Y. Gao, X. Zhang, Upregulation of far upstream element-binding protein 1 (FUBP1) promotes tumor proliferation and tumorigenesis of clear cell renal cell carcinoma. *PLOS ONE* **12**, e0169852 (2017).
46. S. Singer, M. Malz, E. Herpel, A. Warth, M. Bissinger, M. Keith, T. Muley, M. Meister, H. Hoffmann, R. Penzel, G. Gdynia, V. Ehemann, P. A. Schnabel, R. Kuner, P. Huber, P. Schirmacher, K. Breuhahn, Coordinated expression of stathmin family members by far upstream sequence element-binding protein-1 increases motility in non-small cell lung cancer. *Cancer Res.* **69**, 2234–2243 (2009).
47. S. Waaijers, V. Portegijs, J. Kerver, B. B. L. G. Lemmens, M. Tijsterman, S. van den Heuvel, M. Boxem, CRISPR/Cas9-targeted mutagenesis in *Caenorhabditis elegans*. *Genetics* **195**, 1187–1191 (2013).
48. A. Dillin, A. L. Hsu, N. Arantes-Oliveira, J. Lehrer-Graiwer, H. Hsin, A. G. Fraser, R. S. Kamath, J. Ahringer, C. Kenyon, Rates of behavior and aging specified by mitochondrial function during development. *Science* **298**, 2398–2401 (2002).
49. M. Rieckher, M. Markaki, A. Princz, B. Schumacher, N. Tavernarakis, Maintenance of proteostasis by P body-mediated regulation of eIF4E availability during aging in *Caenorhabditis elegans*. *Cell Rep.* **25**, 199–211.e6 (2018).

50. C. M. Phillips, K. L. McDonald, A. F. Dernburg, Cytological analysis of meiosis in *Caenorhabditis elegans*. *Methods Mol. Biol.* **558**, 171–195 (2009).
51. J. Irianto, D. A. Lee, M. M. Knight, Quantification of chromatin condensation level by image processing. *Med. Eng. Phys.* **36**, 412–417 (2014).

Acknowledgments: We thank members of the Tian laboratory members and Q. Bian and for discussion and technical assistance. Several *C. elegans* strains used in this work were provided by CGC [supported by the NIH-Office of Research Infrastructure Programs (P40OD010440)]. **Funding:** This work was supported by the National Natural Science Foundation of China 32225025 and 32321004 (Y.T.), National Key R&D Program of China 2022YFA1303000 (Y.T.), CAS Project for Young Scientists in Basic Research YSBR-076 (Y.T.), New Cornerstone Science Foundation XPLORER PRIZE (Y.T.), National Natural Science Foundation of China 32471212, 32200624 (Q.Z.), China National Postdoctoral Program for Innovative Talents BX2021356 (Q.Z.), and China Postdoctoral Science Foundation 2021 M703474 (Q.Z.). **Author contributions:** Conceptualization: Q.Z. and Y.T. Methodology: Q.Z., H.D., and Y.J. Investigation: Q.Z., H.D., Y.J., Z.W., and J.L. Formal analysis: Q.Z., H.D., and Y.J. Validation: Q.Z., H.D., Y.J., Z.W., and J.L. Visualization: Q.Z. and H.D. Writing—original draft: Q.Z. and H.D. Writing—review and editing: Y.T. and Q.Z. Funding acquisition: Y.T. and Q.Z. Resources: Y.T. Project administration: Y.T. and Q.Z. Supervision: Y.T. **Competing interests:** The authors declare that they have no competing interests. **Data, code, and materials availability:** To obtain all *C. elegans* strains and cell lines created in this study, please contact Y.T. at ytian@genetics.ac.cn. The accession number for the raw sequencing files and the processed data reported in this paper are NCBI BioProject: PRJNA1274529 (https://ncbi.nlm.nih.gov/bioproject/PRJNA1274529), PRJNA1276873 (https://ncbi.nlm.nih.gov/bioproject/PRJNA1276873), and PRJNA1277350 (https://ncbi.nlm.nih.gov/bioproject/PRJNA1277350). Previously published DNA sequence data that were used here are available under accession code PRJNA13758 (https://ncbi.nlm.nih.gov/bioproject/?term=PRJNA13758). All data and code needed to evaluate and reproduce the results in the paper are present in the paper and/or the Supplementary Materials. This manuscript does not report original code.

Submitted 4 October 2025
Accepted 15 May 2026
Published 24 June 2026
10.1126/sciadv.aec8143

Science Advances

FUBL-3/FUBP1 mediates mitochondrial stress–induced chromatin remodeling and longevity

Qian Zhang, Hangyu Dong, Yayun Jiang, Zihao Wang, Jiasheng Li, and Ye Tian

Sci. Adv. **12** (26), eaec8143. DOI: 10.1126/sciadv.aec8143

Science Advances (ISSN 2375-2548) is published by the American Association for the Advancement of Science. 1200 New York Avenue NW, Washington, DC 20005. The title *Science Advances* is a registered trademark of AAAS.